Effects of nanocrystalline and ultrafine grain sizes on constitutive behavior and shear bands in iron

D. Jia [a], K.T. Ramesh [a,*], E. Ma [b]

[a] *Department of Mechanical Engineering, The Johns Hopkins University, Baltimore, MD 21218, USA*
[b] *Department of Materials Science & Engineering, The Johns Hopkins University, Baltimore, MD 21218, USA*

Abstract

The mechanical behaviors of consolidated iron with average grain sizes from tens of nanometers to tens of microns have been systematically studied under uniaxial compression over a wide range of strain rates. In addition to the well-known strengthening due to grain size refinement, grain size dependence is observed for several other key properties of plastic deformation. In contrast with conventional coarse-grained Fe, high-strength nanocrystalline and submicron-grained Fe exhibit diminished effective strain rate sensitivity of the flow stress. The observed reduction in effective rate sensitivity is shown to be a natural consequence of low-temperature plastic deformation mechanisms in bcc metals through the application of a constitutive model for the behavior of bcc Fe in this strain rate and temperature regime. The deformation mode also changes, with shear localization replacing uniform deformation as the dominant deformation mode from the onset of plastic deformation at both low and high strain rates. The evolution and multiplication of shear bands have been monitored as a function of plastic strain. The grain size dependence is discussed with respect to possible enhanced propensity for plastic instabilities at small grain sizes.
© 2003 Acta Materialia Inc. Published by Elsevier Science Ltd. All rights reserved.

Keywords: Nanocrystalline materials; Plastic deformation; Modeling; Shear bands

1. Introduction

Nanocrystalline (nc) materials exhibit extraordinarily high hardness or yield strength [1–11]. A conventional soft metal can acquire a ten-fold increase in strength when the grain size approaches the nanoscale, presumably due to the grain-boundary strengthening known as the Hall-Petch effect.

For example, strengths as high as 1.0 GPa in nc-copper and 2.5 GPa in nc-iron have been reported [1,12,7,8]. Uniaxial compression is a relatively stable testing condition for obtaining substantial plastic deformation [12,8], and this allows for the measurement of the strain-hardening behavior of nc-materials (which often have very limited ductility in tension). Carsley and Milligan performed a systematic study on Fe-10%Cu with grain sizes from 1.6 µm down to 90 nm in compression, and observed nearly perfectly plastic deformation [13,14,5]. Other reported examples of the absence of strain hardening include nc- or ultrafine-grained

* Corresponding author. Tel. +1 41 0516 7735; fax: +1 41 0516 7254.
  E-mail address: ramesh@jhu.edu (K.T. Ramesh).

(UFG) Cu [15,16] and Fe alloys [17,8]. However, there are also counter-examples showing strain hardening in nc metals, e.g. [16,9], particularly at small strains. Although the strain-hardening behavior has long been a topic of interest in conventional materials because of its relevance to tensile ductility and stability, the effect of grain-size on strain hardening in nc-materials remains unclear.

Constitutive models for metallic materials must also account for the effects of the rate of deformation. Significant strain-rate dependence of the flow stress has been observed in many pure metals, particularly at high strain rates. However, very few results have been reported on the high-strain-rate behavior of nc- or UFG materials. Gray et al. [18] tested UFG FCC-Cu, Ni, and Al-4Cu-0.5Zr (prepared using equal channel angular pressing or ECAP) at high strain rates of $\sim 10^{+3}$ s^{-1} with a compression Kolsky Bar, and observed higher strain-rate sensitivity of the flow stress compared with well-annealed coarse-grained metals. Our previous work on an 80 nm-Fe [8] found little strain-rate dependence in the strain rate range from 10^{-4} to $3 \times 10^{+3}$ s^{-1}. The influence of a wide range of grain size on the rate-dependence of the flow stress remains to be systematically explored and understood in terms of deformation mechanisms.

Localized deformation has been reported for nc-metals by several groups; typically this is associated with macroscopic perfect plasticity or even apparent strain softening. Localization of plastic deformation into shear bands was observed in nc-Fe-10%Cu [5] and nc-Fe [8]. Malow et al. observed shear bands in nc-Fe samples after microhardness tests [19]. Shear bands have also been found in a nc-Pd [12] under compression, in a nc-Cu under fatigue [20] and in a nc-Ni under high-rate tension [21]. Our observations in [8] and those of others (e.g. [5]), indicate that there is a transition from uniform to non-uniform deformation as the grain size decreases down to the nanoscale, accompanied possibly by a reduction of strain hardening. The underlying mechanisms associated with this transition are not understood.

The purpose of this paper is twofold. First, we investigate the effects of grain size on the deformation behavior (including strengthening, strain

hardening, and deformation mode) of *bcc*-iron with grain sizes from conventional scales (tens of microns) down to the nanoscale. This wide range is achieved by using a powder metallurgy process. Second, we study the strain-rate dependence of the mechanical behavior of Fe, as a function of grain size, over a wide range of strain rates up to 10^{+4} s^{-1}. Iron was chosen as a model material for this systematic study because it is one of the most common metals, having a basic structure (*bcc*); further, there is a great amount of data in the literature on the mechanical behavior at conventional grain sizes, including data obtained at high strain rates.

2. Experimental procedures

Commercial iron powder with a purity of 99.9% obtained from CERAC Specialty Inorganics Inc. was used as a starting material for ball milling and subsequent consolidation. The powder particles are spheroidal, with a range of sizes averaging around 5 μm. Ball milling [22] was conducted using a SPEX 8000 mill with a vial and balls made of stainless steel (SS440). The typical (weight) ratio of balls/powder was 4:1 and the typical milling time was 18 hrs. The vial was sealed in an argon atmosphere and cooled using a fan during milling. The powder particles after milling have internal grain sizes on the order of 10 nm [22,6], as revealed by X-ray diffraction line broadening. A two-step consolidation procedure was used to form bulk Fe with desired grain sizes. In the first step, the powder was compacted at a pressure of 1.4 GPa at room temperature for about 10 hrs using a tungsten carbide (WC) die set. The resulting compact has a green density of 72–75% of the theoretical density. In the second step, the compact was transferred into a larger WC die set for hot consolidation in an HP20-4560-20 Hot Press. Temperatures in the range of 480–680 °C, consolidation times from 0.5–3 hrs and a pressure of 850 MPa were applied to attain the different grain sizes. Detailed consolidation procedures can be found in [23,24]. The density of each consolidated sample was first determined by measuring its dimensions and weight. The buoyancy method based on the Archimedes Principle was then used for cuboidal

specimens cut from the consolidated samples and polished on all the six surfaces. These two independent methods provided results within 0.5% of each other. The measured relative densities are listed in Table 1. A Vickers Micro-hardness Tester (Leco M-400) was used to measure the hardness of the materials. At least eight indentations were made in each case to obtain the average values in Table 1.

In addition to the average grain size, the distribution of grain sizes is also an important variable. For the UFG-/nc-Fe, TEM examinations in a Philips 200 (including bright field, dark field, and diffraction pattern) were performed to characterize the microstructures, with samples prepared using the standard polishing, dimpling and ion milling (0.5 mA, 5 kV Ar) procedures. For the coarse-grained samples, an optical microscope and scanning electron microscope were used. Most of the grain sizes listed in Table 1 were determined by number-averaging more than 350 grains. Two typical TEM micrographs for the average grain sizes of 138 and 268 nm are shown in Figs. 1(a) and (b) respectively. No heavy textures were observed. The corresponding grain size distributions for these two cases are shown in Figs. 1(c) and (d). While there are relatively few large grains in these distributions, the largest grains may have a disproportionate effect on the deformation mode (see discussion in Section 4).

Compression tests were performed to obtain full stress-strain curves over a wide range of strain rates. In order to minimize data scatter from sample to sample, all of the specimens for the mechanical tests were cut using an electric discharge machine from the same consolidated sample for each grain size of interest (the orientation for mechanical loading was always along the axis of the consolidated circular cylinder). The typical specimen dimensions for the low and high strain rate tests are $2.2 \times 2.2 \times 3.5$ mm (length) and $1.6 \times 1.6 \times 1.4$ mm (length), respectively. The influence of specimen geometry was independently evaluated. The reason for choosing prismatic (rather than cylindrical) shapes for the specimens is not only that a greater number of specimens can be cut from a single consolidated sample, but also for convenient observation of possible shear bands on the flat surfaces. Compression tests at quasistatic strain rates of $1-2 \times 10^{-4}$ s^{-1} were performed using a screw-driven ATS machine. Two tungsten carbide platens (with polished-mirror surfaces) were used and lithium grease was applied at the two specimen/platen interfaces to reduce the interfacial friction. Dynamic compression tests at strain rates of the order of 10^{+3}–10^{+4} s^{-1} were performed using a miniaturized Kolsky Bar technique [25] specially developed for the purpose of dealing with these small samples. Samples were recovered after dynamic loading for microscopic analysis.

If failure occurred in compression, the failure mechanisms were evaluated through visual and microscopic observations. The two parallel flat loading surfaces of each specimen were produced using a LapMaster lapping machine with an Accupol fixture. The four lateral surfaces were polished using a precision polishing machine and a tripod to flatness and surface finishes of 0.5 µm. The last polishing scratches were oriented along the loading direction to serve as markers for easy identification of shear bands. During quasistatic loading a careful visual observation of deformations on the well-pol-

Table 1
Density, hardness and grain sizes obtained at indicated conditions

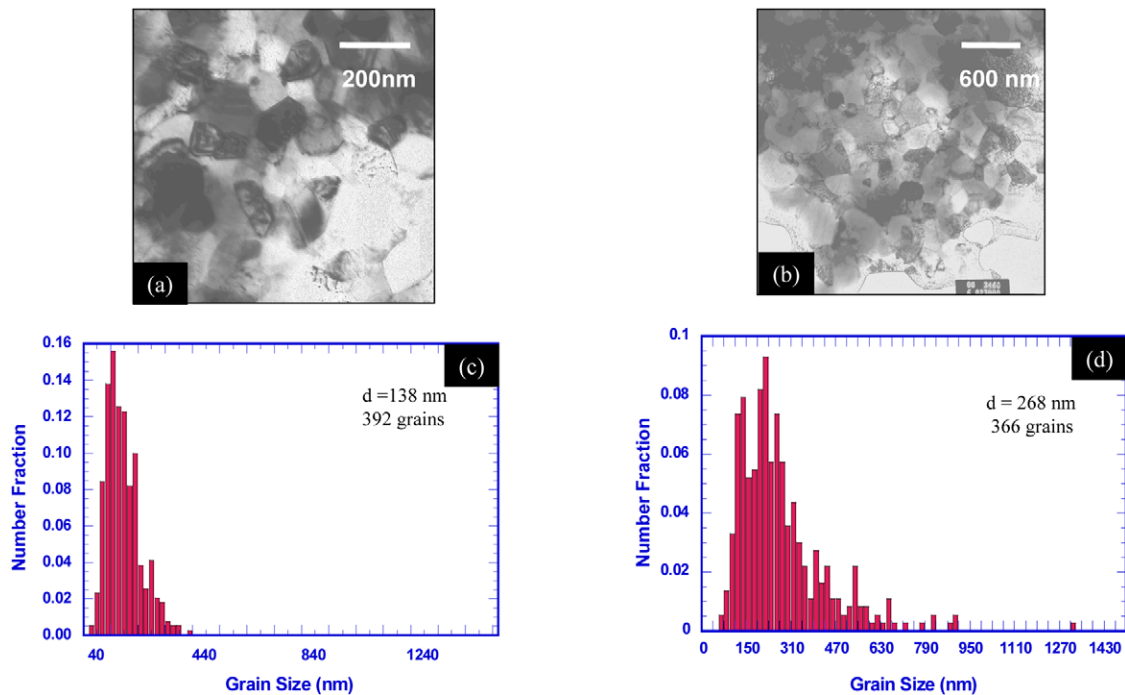| Consolidation temperature and time	Relative density (%)	Hardness (VHN)	Average grain size (nm)
410 °C, 30 min	99.2	654	80
500 °C, 3 hrs	99.0	592	138
590 °C, 3 hrs	99.4	437	268
680 °C, 3 hrs	99.3	247	980
590 °C, 3 hrs	99.1	134	20,200
1100 °C, 3 hrs (annealing)			

Fig. 1.   TEM micrographs of the iron samples consolidated at (a) 500 °C for 3 hrs, bright field image, and (b) at 590 °C for 3 hrs, dark field image. The grain size distributions corresponding to the materials in (a) and (b) are shown in (c) and (d) respectively.

ished side surfaces was made for each specimen, while observations with an optical microscope were performed after each test. TEM studies of the failure micromechanism were performed post-mortem on several of the specimens from each loading condition using a tripod polishing technique.

3. Deformation behavior and failure

3.1. Mechanical behavior

3.1.1. Quasi-static compression

The solid lines in Fig. 2 show the true stress-strain curves of the consolidated iron with various average grain sizes obtained from the quasistatic compression tests. It is apparent, first of all, that the strength (yield strength or flow stress) increases with decreasing grain size. Compared with the 20 μm-Fe, the strength of the nano-Fe (80 nm) is increased by an order of magnitude. Second, the strain hardening rate (the slope of the stress-strain
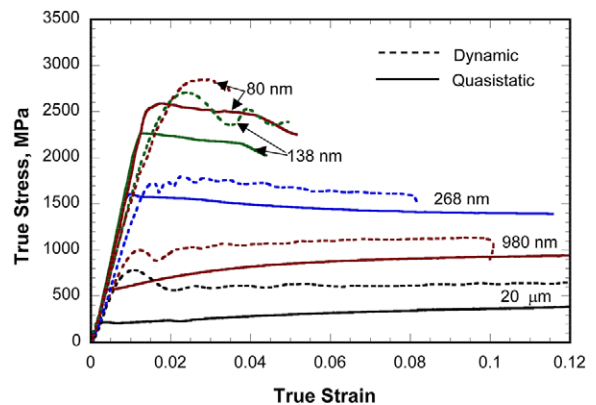

Fig. 2.   Typical stress-strain curves obtained for the consolidated iron under quasistatic (1–4×10^{-4} s^{-1}) and high-strain-rate (3–$6 \times 10^{+3}$ s^{-1}) uniaxial compression for all of the grain sizes.

curve) changes with the grain size. In the range of grain size from 20 μm to 980 nm, there is no marked change in the slope of the curves. However, there is a transition from strain hardening to

apparent strain softening as the grain size changes from ~1 μm to ~300 nm. For grain sizes below 300 nm, apparent strain softening appears at a very low plastic strain (if not immediately following the onset of yielding). Third, while ductile behavior is observed at relatively large grain sizes, the samples with grain sizes smaller than 200 nm fail relatively early (the stress-strain curves presented end because of specimen failure). In sum, strong effects of grain size are observed in terms of strength, apparent strain hardening, and failure. For bcc metals we do not expect to have a significant effect of grain size on the strain hardening (see Section 3.2), and so these observations indicate that a change of deformation mechanism has occurred at the smaller grain sizes (conceivably leading eventually to the failures observed).

The measured flow stresses (at a fixed strain of 4%) and the yield strengths estimated from the VHN are observed to satisfy the well-known Hall-Petch relationship ($\sigma_y = \sigma_o + \beta d^{-1/2}$), including results for a pure iron with a very large grain size ($d = 70$ μm) from [26]). The Hall-Petch constant β is 0.69 MPa m$^{1/2}$ for flow stress (this is very similar to the value obtained for this parameter in [27] for conventional α-Fe). The grain-size dependent strength is also consistent with results on the Fe powder [1,22] and tensile results on a bulk Fe [10].

3.1.2. High strain rate compression

Fig. 2 also shows a set of stress-strain responses at high strain rates of $3 \times 10^{+3}$–$6 \times 10^{+3}$ s^{-1} (the dashed lines), together with the corresponding quasistatic curves (the solid lines) for each grain size. Strain-rate hardening is evident for all of the grain sizes considered. Little influence of the strain rate on the strain hardening (the slope of the curves) is observed, which is typical for bcc metals (see Section 3.2). The ends of the high-rate stress-strain curves for the smallest two grain sizes represent specimen failures rather than unloading. The oscillations in the early parts of the high-strain-rate curves are a consequence of the experimental technique, and so do not represent material response.

The influence of the rate of deformation on the flow stress is plotted in Fig. 3 for the entire range of grain sizes and strain rates, using a conventional
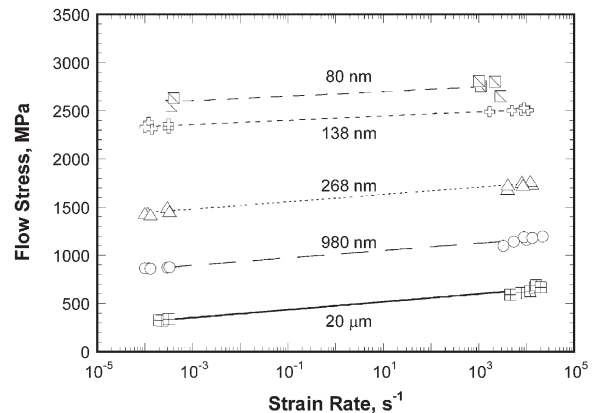

Fig. 3. Rate dependence of the flow stress of the consolidated iron for each grain size, with the flow stresses plotted at a fixed strain of 4%.

semi-log format, with the flow stresses plotted corresponding to a fixed strain of 4%. Examining first the response of the conventional (20 μm) grain size material, we see that the strength almost doubles over this range of strain rates, with the influence of strain rate somewhat higher at the highest rates. Such a response is normally observed in bcc metals, e.g. [26]. The smaller grain size materials are much stronger at low rates, but show less relative strengthening at high strain rates. An approach to understanding grain size effects on strain hardening and strain rate sensitivity of the flow stress for bcc Fe is presented in the following subsection.

3.2. Constitutive modeling

For the grain size range (80 nm–20 microns) of interest here, dislocations are the main carriers of plastic deformation. Screw dislocation cores are dissociated into non-planar configurations in bcc structures [28], and the mobility of the edge components of dislocation loops is much higher than the mobility of the screw components. Recent calculations manifesting degenerate screw cores for bcc-Fe are presented by Ngan and Wen [29]. It has been established that in bcc metals the primary barriers to the motion of the screws are lattice-related Peierls barriers. The screw dislocations themselves move by the nucleation and propagation of kink pairs; at low temperatures, screw

mobility is primarily controlled by kink nucleation. The kink pair nucleation rate ν_k is given by

$$\nu_k = \nu_{k0}\exp\left(-\frac{\Delta G_k}{kT}\right) \qquad (1)$$

where ν_{k0} is the attempt frequency and ΔG_k is the activation energy for kink-pair nucleation [30,31]. The corresponding average dislocation velocity is

$$\nu_d = \lambda\nu_k = \lambda\nu_{k0}\exp\left(-\frac{\Delta G_k}{kT}\right) \qquad (2)$$

where λ is the distance between the Peierls barriers (of the same order as the Burgers vector b in bcc metals). The plastic rate of deformation corresponding to this mechanism is then

$$\dot{\gamma} = \rho_m b\lambda\nu_{k0}\exp\left(-\frac{\Delta G_k}{kT}\right) \qquad (3)$$

where ρ_m is the mobile dislocation density (assumed constant in Eq. (3)) and b is the Burgers vector. A Taylor factor of the order of 3 has been absorbed into the assumed value for the mobile dislocation density in Eq. (3), since ρ_m is usually only known to within an order of magnitude in any case.

The key remaining question is the dependence of the activation energy on the stress. A common approach to this definition of the barrier shape is to use an empirical function first proposed by Kocks, Argon & Ashby (KAA) [32]:

$$\Delta G_k = \Delta G_{k0}\left\{1-\left(\frac{\hat{\tau}}{\bar{\tau}_0}\right)^p\right\}^q \qquad (4)$$

where p and q are parameters that define the barrier shape, $\hat{\tau}$ is the effective stress for this thermally activated mechanism and $\bar{\tau}_0$ is a material parameter. Various values for p and q are used in the literature; particularly common values used for bcc metals are $p = 1/2$, $q = 3/2$. Using Eq. (4) in (3) and solving for the stress, the effective thermally assisted "Peierls stress" $\hat{\tau}$ is then given by

$$\hat{\tau} = \bar{\tau}_0\left[1-\left\{\frac{kT}{\Delta G_{k0}}\ln\left(\frac{\rho_m b\lambda\nu_{k0}}{\dot{\gamma}}\right)\right\}^{\frac{1}{q}}\right]^{\frac{1}{p}}. \qquad (5)$$

The collection of microscopic terms in the numerator of the logarithmic function is sometimes referred to as a "reference" strain rate $\dot{\gamma}_{0k} =$

$\rho_m b\lambda\nu_{k0}$. Considering typical values for these parameters for an annealed metal, we see that $\dot{\gamma}_{0k} \gtrsim 10^5\ s^{-1}$ (although usually many orders of magnitude larger).

The effective Peierls stress $\hat{\tau}$ is the component of the flow stress τ related to thermally activated motions over the short-range barriers (corresponding to the Peierls barriers in this case). To develop the constitutive function for the material we need to add to this the "athermal" stress corresponding to that needed to overcome the long-range barriers perceived by the moving dislocations, i.e. $\tau = \tau_{\text{athermal}} + \hat{\tau}$, so that we obtain the flow stress as

$$\tau = \tau_{\text{athermal}} + \bar{\tau}_0\left[1-\left\{\frac{kT}{\Delta G_{k0}}\ln\left(\frac{\dot{\gamma}_{0k}}{\dot{\gamma}}\right)\right\}^{\frac{1}{q}}\right]^{\frac{1}{p}} \qquad (6)$$

The primary part of the athermal stress (i.e. the most important long-range barriers) for the materials that we are considering will be that arising from the grain boundaries, and this brings in a grain size dependence that we assume to be of the Hall-Petch form:

$$\tau_{\text{athermal}} = \tau_{a0} + \beta d^{-1/2} + g(\gamma). \qquad (7)$$

Here we have also included a strain hardening function $g(\gamma)$ in an additive fashion, since experimental evidence for bcc metals generally indicates that the strain hardening function is not affected by strain rate or temperature in the low-temperature regime, e.g. [33]. We now have an effective response function that should be applicable to our bcc iron:

$$\tau = \tau_{a0} + \beta d^{-1/2} + g(\gamma)$$
$$+ \bar{\tau}_0\left[1-\left\{\frac{kT}{\Delta G_{k0}}\ln\left(\frac{\dot{\gamma}_{0k}}{\dot{\gamma}}\right)\right\}^{\frac{2}{3}}\right]^2 \qquad (8)$$

using the common *bcc* values for p and q in Eq. (4). By replacing $\hat{\tau}$ with the effective stress $\sigma_e = \sqrt{J_2}$ and $\dot{\gamma}$ with the effective plastic strain rate, we obtain a constitutive formalism that we can use to compare with our experimental results.

The key feature of Eq. (8) for our purposes arises from the assumed mechanism of plastic deformation in bcc metals—we should expect that the change of grain size will not affect the additive stress term corresponding to the rate-sensitive

response of the material. In terms of our experimental results, Eq. (8) tells us that it is useful to examine the variation with strain rate of the rate-dependent term alone as in Eq. (5) (i.e., we examine the flow stress difference $\sigma_f - \sigma_{f0}$, where σ_{f0} is the average flow stress for each grain size measured at the low rates) since the effect of grain size and strain represent additive terms for the assumed deformation mechanism. The flow stress difference is plotted as a function of the strain rate in Fig. 4, and indicates that the behaviors of these different grain size materials are quite consistent (given the scatter in the data with the 80 nm material). The data on the 138 nm material has less scatter, and this material does appear to develop less strain rate hardening. However, the observations of failure mode presented in the next section indicate that the failure mechanism may have a stronger influence on the results for the smallest grain sizes than the slip-level deformation mechanism.

The solid curve in Fig. 4 represents Eq. (5) with $p = 1/2$, $q = 3/2$ and specific material parameters as follows. We assume that $\rho_m \sim 10^{15}\ m^{-2}$; the Burgers vector b is on the order of $3x10^{-10}\ m$; the attempt frequency v_{k0} is $\sim 10^{12}\ s^{-1}$ and the operating temperature is 300 K. A value of 0.675 eV for ΔG_{k0} is consistent with values reported from atomistic simulations [34,29] in *bcc* metals. The remaining parameter that must be fit is the reference stress $\bar{\tau}_0$; a value of 1.2 GPa for $\bar{\tau}_0$ provides the curve shown in Fig. 4. The model is able to

capture the primary features of the observed behavior using physically reasonable parameters for this strain rate and temperature regime.

Although the absolute increases in strength as a result of changes in strain rate are consistent across these grain sizes in accord with the model predictions, the *relative* rate-dependent strengthening of the nc-Fe is much smaller than that observed at conventional grain sizes, so that the total flow stress is less sensitive to strain rate in the UFG-/nc-Fe. This is illustrated in Fig. 5, which plots the normalized flow stress (normalized by the flow stress at quasistatic rates of deformation) as a function of the strain rate. The effective rate-sensitivity of these materials (as described, for example in the index of a power-law rate-dependence function) decreases as a function of grain size because the dominant part of the strength is the grain boundary strengthening at small grain sizes. For example, if one were to use a power-law rate-dependent function (the curves in Fig. 5) to describe the effective response ($\sigma/\sigma_0 = [\dot{\varepsilon}/\dot{\varepsilon}_0]^m$, a form commonly used in finite element codes), the strain rate hardening index m decreases by as much as an order of magnitude (from 0.04 for the 20 μm material to a negligible 0.004 for the 80 nm material) as σ increases by an order of magnitude over this grain size range. This reduction in effective rate sensitivity may have implications for the stability of the deformations in nanostructured materials, given that
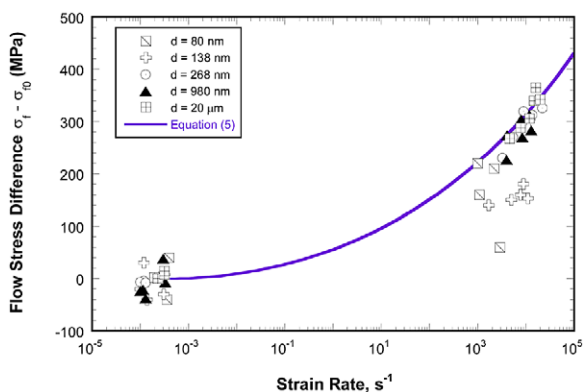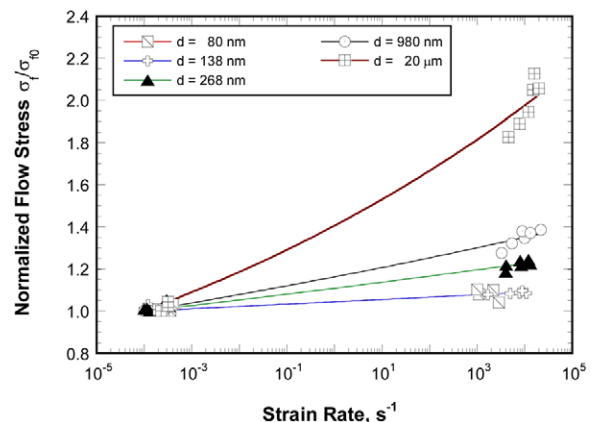

Fig. 4. The rate dependence of the flow stress difference ($\sigma_f - \sigma_{f0}$) for the various grain sizes, together with the predictions of the constitutive model.

Fig. 5. The variation of the normalized flow stress (σ_f/σ_{f0}) with strain rate for the various grain sizes. Note the reduction in the effective rate sensitivity at the smaller grain sizes.

these high strength materials also typically have low strain hardening (note, however, that moderately increased rate sensitivity has been observed in nc-Ni [21] and nc-Cu [35]).

3.3. Failure mechanisms

3.3.1. Phenomenology of shear bands

The deformation mode of these materials changes dramatically as the grain size is decreased into the ultra-fine-grain range. In the 20μm-Fe and 980nm-Fe, the compressive deformations were uniform at all strain rates and no shear bands were evident under either the optical microscope or SEM (note that no twins were observed in these materials even at high strain rates). However, for all smaller grain sizes ($d < 300$ nm) shear band development was observed to occur immediately after the onset of plastic deformation, correlating to the observed change in apparent strain hardening at those grain sizes. Shear bands were observed during both quasistatic and high-rate deformations for these grain sizes. Comparative optical micrographs are presented in Fig. 6 after low-rate compressive deformations to similar plastic strains, showing (a) the uniform deformations in the 980 nm-Fe and (b) the strongly non-uniform deformations in the 268 nm-Fe. Shear band populations similar to Fig. 6(b) were observed in all specimens with grain sizes $d < 300$ nm. Fig. 6(c) shows the

strongly non-uniform deformations observed in the 268 nm-Fe after high-rate loading to a similar strain as in Figs. 6(a) and (b).

The process of development of these shear bands was studied using "progressive" low-rate compression tests performed on the 268 nm-Fe with repeated loading/unloading/reloading at controlled nominal levels of strain. The evolution of the shear band population over an entire specimen as a function of strain is presented in [36]. As shown there, the onset of plasticity corresponds to the appearance of shear bands emanating from one of the edges of the specimen (which is not necessarily on the moving side in any given experiment). It was demonstrated in [36] that additional shear bands appear with increasing strain and that the newly generated shear bands have similar orientations (in the four possible shearing planes for these cuboidal specimens). Large numbers of shear bands are observed, rather than single dominant bands that lead to failure.

The process of shear banding that develops during a quasistatic experiment can be observed in Fig. 7, which shows a single area (well away from the edges) of a 268 nm-Fe specimen at nominal plastic strains of (a) 3.7% and (b) 7.8%. The loading axis is vertical in these figures. The straight lines produced by the directed polishing described earlier are visible in both figures and may be used to deduce the amount of shear in each band as the
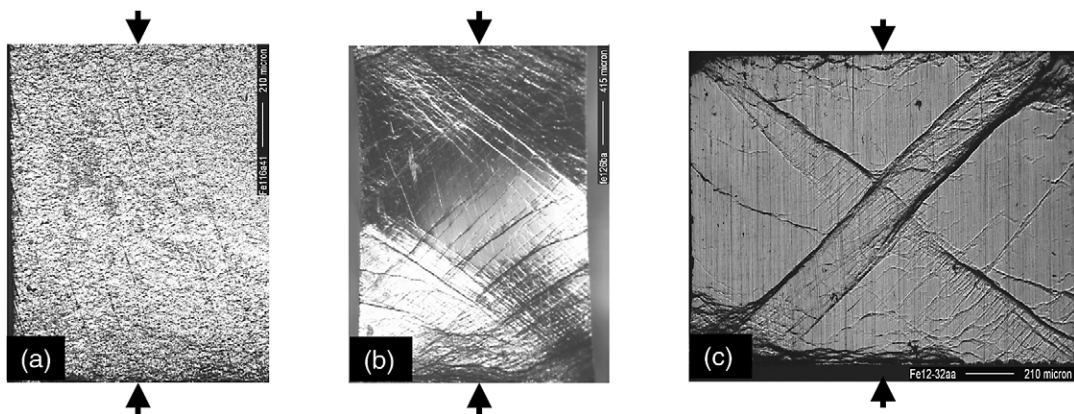

Fig. 6.   Change in deformation mode of consolidated iron with grain size for uniaxial compression: (a) uniform low-rate deformations with $d = 980$ nm, $\varepsilon = 13.7\%$; (b) non-uniform low-rate deformations with $d = 268$ nm, $\varepsilon = 11.6\%$ and (c) non-uniform high-rate deformations with $d = 268$ nm.
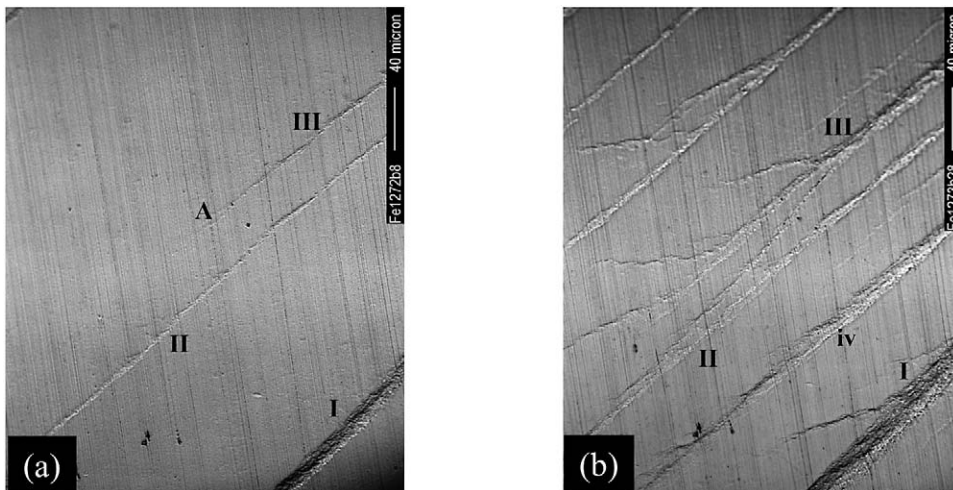
Fig. 7. Evolution and development of shear bands in 268 nm-Fe. Observations of shear bands at the same location at different nominal strain levels: (a) 3.7%; (b) 7.8%. Loading axis is vertical. Note the development of new shear bands, the broadening of existing shear bands, and the propagation of a shear band tip.

nominal strain develops. Three shear bands denoted I, II and III are visible in Fig. 7(a), including one band tip denoted by A (note that band tips are atypical in our data in unconfined regions). By the time the nominal plastic strain has reached the level of 7.8% in Fig. 7(b), a minimum of eight shear bands are visible (i.e., five new bands have appeared). Bands I, II and III are all considerably broader (Band I, for example, has grown in width by more than 50%). Band III has propagated, including several branches, one of which has apparently merged with Band II. Interestingly, one of the new bands (Band iv) is at least as broad as the current size of Bands II and III, indicating that the deformation within a newly nucleated band can be substantially larger than that in an existing band. Tracing the polishing lines, one observes that the total strain in Band I has increased. Observations with optical microscopy and TEM for the deformed UFG-/nc-Fe specimens show that large plastic deformations are developed within the bands [36]. Thus, it appears that the process of shear banding in this material involves the nucleation of new bands, propagation along the shear plane, increase in width (broadening) and increase in strain (flow) within the band.

Fig. 8(a) shows a high-magnification view of a single shear band with well-defined boundaries

(this band was observed at a nominal plastic strain of 0.3%, just after yield). The shear deformation within the band can be traced by following a polishing scratch across the band. The measured width of the shear band in Fig. 9(d) is ~16 μm and the shear strain in the band is ~25% (nearly two orders of magnitudes higher than the nominal specimen strain).

Although no shear bands are present along the conjugate planes in Fig. 7, the bulk of the specimen develops shear bands along more than one of the conjugate planes so that shear band intersections are common and remarkably organized networks of shear bands are observed. Fig. 8(b) shows a network of shear bands at about ±45° to the loading axis in a 268 nm-Fe specimen after low-rate loading to 7.8% nominal plastic strain. The relative uniformity of the shear band spacing may provide clues for models of this failure mode. The intersections of shear bands are observed to remain compatible within optical resolution (we have been unable to capture a shear band intersection within the TEM with our tripod-polishing techniques).

For most of the bands, the two boundaries can be clearly identified, so that the width can be accurately measured (Table 2). The band widths listed in Table 2 (all measured using the optical microscope) for the 138 nm- and 268 nm-Fe are
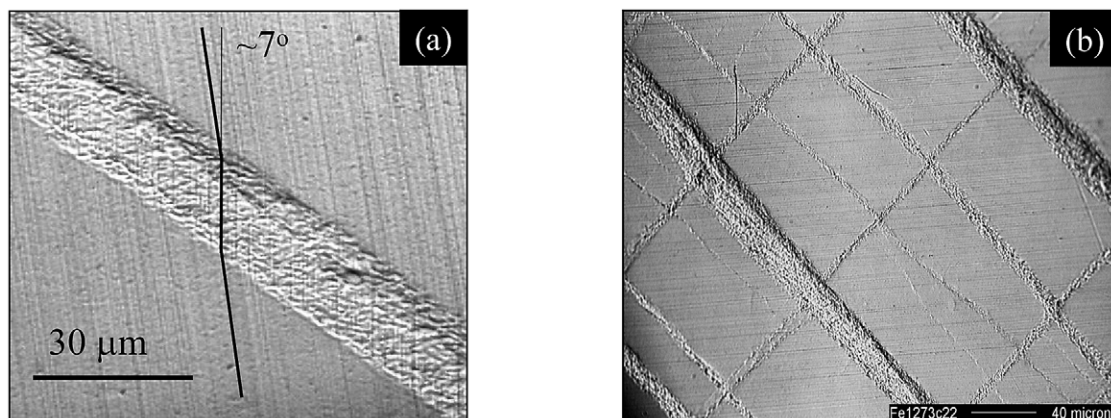
Fig. 8. (a) Shear strain developed in shear band immediately after onset of plastic deformation (0.3% plastic strain) in 268 nm-Fe under uniaxial compression. (b) Shear band network formed in 268 nm-Fe after uniaxial compression at low rates to 7.8%. Note the compatible deformations at the intersections of the shear bands.
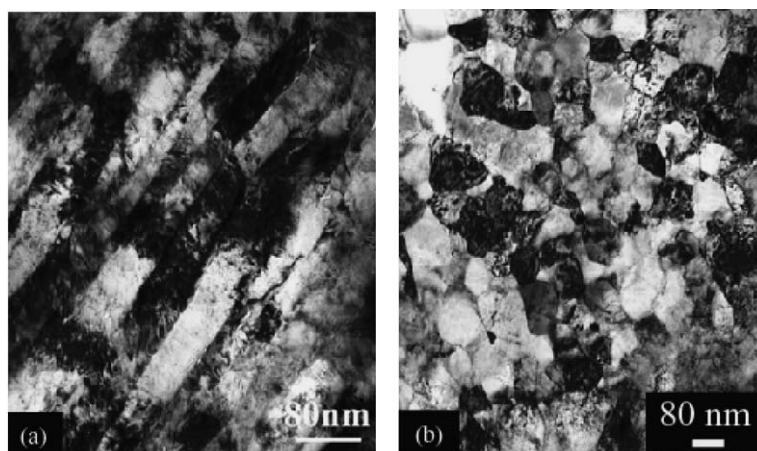

Fig. 9. TEM micrographs taken within (a) and (b) and outside (c) and (d) a shear band in 138 nm-Fe. Note the equiaxed grains outside the band, and the elongated grains in the band oriented along the shear direction.

Table 2
Thickness of shear bands

Grain size d (μm)	0.08	0.138	0.268
Band width w (μm)	4.6	6.8	16.4
Size ratio $R = w/d$	58	49	61

the thickest bands observed at low plastic strains ($<0.5\%$) while that for the 80 nm-Fe is the thickest band observed at a plastic strain of 2.3% after unloading (tests at a lower plastic strain were not performed on the 80 nm-Fe). Wider bands were observed in the 268 nm-Fe than in 138 or 80 nm-Fe. In contrast, the band-width/grain-size ratio, R, for all the three grain sizes remains similar, on the order of 50, as seen in Table 2. In all the three UFG-/nc-Fe, the orientations of most bands

(defined as the angle between the normal to the shear band plane and the loading axis) were 41–46°, suggesting that the orientations are insensitive to grain size.

The shear band thickness values listed in Table 2 are the maximum measured widths for a *single* band at low strain levels (<2.5%). At sufficiently high strains, numerous bands may group into "shear zones" (two diagonal shear zones can be seen in the dynamically loaded specimen of Fig. 6(c)). The boundaries of the bands in the zones become more difficult to identify whereas the boundaries of the zones remain clear. The development of the zones is affected by the specimen aspect ratio, because of kinematic constraints from the specimen ends. The maximum width of the shear band zones measured in the 268 nm-Fe at a plastic strain of 7.8% is 158 μm, which is close to the results on the Fe-10%Cu reported by Carsley [14] for a similar grain size.

3.3.2. Microstructure within shear bands

TEM observations of the shear bands were made using a tripod-polishing technique (details in [36]). An example of the TEM results is presented in Fig. 9, which shows TEM micrographs obtained from outside and within shear bands in 110 nm-Fe deformed in compression at low rates. Fig. 9(a) is a typical picture obtained from within the shear band, and shows elongated grains (elongated along the shearing direction) containing high dislocation densities. Fig. 9(b) was obtained from a region outside the shear bands, and shows equiaxed grains. The grains inside the band (Fig. 9(a)) show evidence of texturing involving the activation of <111>/[37] slip systems [36]. There is no evidence of recrystallization within the shear bands, and the shear band boundaries are relatively sharp. Further, no gradient of microstructure is observed across the shear bands.

3.3.3. Effect of strain rate on the failure mechanism

High-strain-rate experiments were also performed with controlled strain (by choosing the length of the projectile and the initial velocity). For all the recovered specimens (in which the plastic deformation was caused only by a single well-

characterized loading), optical micrographs were taken of the side surfaces. For a similar strain level, the distribution of shear bands is more uniform in the low-rate specimens (Fig. 6(b)) than in the high-rate specimens (Fig. 6(c)), but that arises primarily because of the differences in specimen aspect ratio (note the shear zones in Fig. 6(c)). The shear band orientations and widths, however, remain similar. Although our TEM data on the high-rate specimens is more limited, our TEM observations at high rates do not differ qualitatively from those presented so far. No macroscopic shear bands were observed in the 20 μm-Fe or 980 nm-Fe loaded at high-strain rates. In summary, the basic mechanism of shear banding does not appear to change between the low-rate and high-rate loading; the failure mechanism appears to be mediated by grain size rather than strain rate. This indicates—together with the microstructural evidence of Section 3.3.2 and [36]—that the bands observed here are not adiabatic shear bands.

3.3.4. Effect of specimen geometry on the failure mechanism

A number of short specimens (with the same aspect ratio as that used for the high-strain-rate tests) were also tested at low strain rates to examine possible effects of the different specimen geometries conventionally used in such tests. In the 20 μm-Fe and 980 nm-Fe, which deform uniformly like conventional ductile metals, no effects of specimen geometry were observed on the stress-strain behavior. There was also no significant difference in the observed stress-strain curves for the long and short specimens of 268 nm-Fe, even though the shear band mechanism is active at this grain size. The specimens (both long and short) were able to sustain very large deformations without failure. Note that the slight upturn in the stress-strain curves is observed for both long and short specimens. The experiments on the 138 nm-Fe showed that the yield strengths and the orientations of the shear bands were identical for the long and short specimens, but the total strain to catastrophic failure was much larger for the short specimens (as is expected, because of the effective constraint provided by the compression platens in the small aspect ratio case). In summary, the grain sizes at

which the shear band mechanism is observed, the stress levels at which the shear bands are formed, the orientations of the shear bands, and the morphology (width, microstructure) of the shear bands all appear to be independent of specimen geometry. However, the strain to failure in our experiments is modulated by the specimen geometry because of the shear band mechanism.

4. Discussion

4.1. Implications for the effective ductility of nc-materials

The grain size dependence of strain hardening for these small grain sizes is complicated by the fact that the shear band mechanism becomes active for $d < 300$ nm. If we consider the overall response of these materials, it appears that the strain hardening rate h (defined as the current slope $h = (\partial\sigma/\partial\varepsilon)|_{\dot{\varepsilon}}$ of the true stress vs. true strain curve obtained at a fixed strain rate) decreases dramatically for $d < 300$ nm. As a consequence of this and the increase in flow stress with reduced grain size, the strain hardening index q (defined as $q = h/\sigma$; note that for power-law strain hardening we have $q = (h/\sigma) = (n/\varepsilon)$ where n is the strain hardening exponent) decreases with decreasing grain size. Consequently, failure is expected to occur more easily in tensile tests of nanocrystalline materials. This is consistent with the tensile results reported by Takaki et al. [10] for a bulk iron with grain sizes smaller than 300 nm, where necking commences at very small plastic strain after yielding. Note that in the samples used in this paper, prepared by hot consolidation, the high dislocation density from cold work has been converted to grain boundaries due to recovery and recrystallization. Therefore, what we observe are grain boundary effects, not just the effects of heavy cold work. We have also observed a dramatic reduction of h along with enhanced σ in an UFG pure Ti relative to conventional Ti [38]. Note that q is reduced even when moderate h remains, as reported for a nc-Cu [9] and a few other nc-*fcc* metals [39]. From these and other reports in the literature it appears that the strain hardening index q is strongly depressed

when the grain size reaches the UFG/nc-regime. The increase in strain rate hardening due to grain boundary deformation mechanisms is insignificant except perhaps for extremely small nc grain sizes or materials with relatively low melting points. The lack of strain hardening, compounded with the diminishing effective strain rate hardening that we observe, enhances the propensity for plastic instabilities, such as the initiation and propagation of shear localization and necking in tension [38]. This is often exacerbated by impurities and porosity as a result of the particular processing route used to make the nc/UFG material.

4.2. Comparisons with granular and amorphous materials

Shear bands are also seen in the compressive deformations of granular materials such as sands, and it is tempting to compare powder-consolidated systems with granular materials. A key microscopic difference is that the contact area of two sand grains is much smaller than the corresponding contact area in the UFG-/nc-Fe. Further, the microstructures of our materials (Fig. 9) are typical of those of plastically deforming polycrystalline metals. There is also no sign of significant void formation or dilatation at the intersection of shear bands. The band-width/grain-size ratio $R = w/d$ values (of the order of 50) seen in Table 2 are higher than those observed in granular materials such as various sands, which are typically in the range of 10–30 (see, e.g. [40,41]). Note that most of the size ratios reported for sands were measured at the peaks of the load-displacement curves while our results were for small strain levels *after* the peaks, and bands become wider with increasing strain during the process of plastic flow. With smaller contact area and high porosity, shear bands in sands should occur with fewer particles (in the band thickness direction) involved. In addition, while in sands little plastic deformation occurs inside the grains, in our samples dislocation activity is substantial in addition to any rotation/sliding of the grain as a whole [42,43]. Computational analyses have indicated that dissipative mechanisms such as plasticity and friction

are likely to increase the band width to grain size ratio.

Shear bands are also common in amorphous alloys and their composites (see, e.g. [44])—these materials are considered by some to represent the limit of zero grain size. The thickness of a shear band in amorphous alloys is on the order of 10–20 nm [45], and the band width/atom-size ratio is also roughly 50–100. However, to the authors' knowledge, broadening of shear bands does not occur in amorphous metals with increasing plastic strain.

4.3. Proposed mechanism for shear bands in nanostructured metals

We propose here a conceptual mechanism that would lead to the shear bands observed in these experiments. A key feature of our observations is the development of shear bands only in materials with sufficiently small grains. The transition from uniform deformation to non-uniform deformation below a certain grain size, accompanied by a change from overall strain hardening to overall strain softening, suggests the onset of a different underlying deformation mechanism possibly involving grain boundaries [42,43] or grain rotations.

As the applied stress increases, substantial plastic deformation occurs preferentially initially at the occasional large grains that exist in these materials (see the grain size distribution of Fig. 1 for the 268 nm-Fe), since the surroundings of these grains are effectively stronger. We hypothesize that when the applied stresses reach sufficiently high values, it becomes possible to reorient the much smaller grains surrounding the large soft grain into orientations that are much more suitable for shearing, and the associated geometric softening triggers the shear localization (Fig. 9, and [36]). Note that as the average grain size increases, it becomes more difficult to reorient a sufficient number of grains to trigger the geometric softening mechanism (although this might still occur at larger defects, such as inclusions or cracks). Once triggered, plastic deformation develops within the now preferentially oriented grains in the shear band (Fig. 9), and the associated local work hardening leads to the

broadening of the band with increasing plastic strain (local work hardening is assumed to continue even though no macroscopic hardening is observed). In a strain rate controlled experiment, additional shear bands are triggered in order to provide sufficient plastic deformation to maintain the imposed global plastic strain rate, provided there are sufficient nucleation sites. Assuming that a log-normal distribution is a reasonable description for the grain size distribution, and considering the measured grain size distributions of Fig. 1, we conclude that there are very large numbers of soft large grains available for nucleation of shear bands and so the abundance of nucleation sites is not an issue. Since there are so many possible sites for such microscopic geometric softening, shear band orientation would be determined (as observed) by the macroscopic stress state rather than by the specific locations of defects in the microstructure. This hypothesized geometric softening mechanism can operate at both the low and high rates of deformation considered here, although the additional component of a temperature rise at high strain rates might accentuate the softening component. The hypothesized mechanism would indicate that the grain size distribution would play a significant role in whether or not the shear band mechanism is observed in these fine-grained materials.

The observed band widths indicate that there are very large numbers of large grains in the volume of a single shear band, given the band width to grain size ratios measured in Table 2. Examining the grain size distribution shown in Fig. 1 for the 268 nm-Fe, we note that there was one grain with a diameter of ~1.3 μm and 3 grains of ~0.9 μm in the 366 grains counted. For a 16 μm thick shear band (Table 2) in a typical quasi-static test specimen of the 268 nm-Fe material, there are approximately $2.4 \times 10^{+9}$ grains. It follows that a single shear band would contain several million grains with a diameter >1 μm (note that such a great number of coarser grains could also contribute to the observed band width to *average* grain size ratio).

Quantitative analysis of the effectiveness of such geometric softening as a mechanism for the development of the observed shear bands requires a full polycrystalline model that handles both the plastic

anisotropy of the material and the grain size distributions. Theoretical modeling might also be able to describe the observed trends in band width and band spacing, and will be pursued in subsequent work.

5. Conclusions

As the grain size is decreased into the ultrafine and nanocrystalline regime in consolidated Fe, we observe strong effects of grain size on the constitutive response and on the microscopic deformation mode. The following points summarize our results:

1. The effective yield stress increases with decreasing grain size in a manner consistent with the Hall-Petch relationship, and the grain boundary strengthening becomes the dominant part of the flow stress. The effective strain hardening decreases, becoming negligible for grain sizes $d < 300$ nm. This change correlates directly with a change in the deformation mode from uniform deformations at large grain sizes to localized shearing deformations for $d < 300$ nm. Shear bands are observed even at quasistatic strain rates and low strains, and become the dominant mode of plastic deformation.
2. A physically-based constitutive model has been developed that describes the rate-dependent behavior of bcc iron over the range of strain rates from 10^{-4} s^{-1}–10^{+4} s^{-1}.
3. The effective rate sensitivity decreases with decreasing grain size in the UFG/nano grain size regime for this bcc metal. The influence of grain size on the rate-dependence of the flow stress is qualitatively consistent with current understanding of deformation mechanisms in bcc metals.
4. The observed strain hardening (or lack thereof) remains consistent between quasistatic and dynamic loading. The basic mechanism of shear banding does not appear to change between the low-rate and high-rate loading; the failure mechanism appears to be mediated by grain size rather than strain rate. The microstructure within the shear bands does *not* appear to be consistent with adiabatic shear band mechanisms.

5. The process of shear banding (under compression) in this material involves the nucleation of new bands, propagation along the shear plane, increase in width (broadening) and increase in strain (flow) within the band. Networks of shear bands are observed at larger plastic strains. The shear band widths observed are at least 50 times the grain size at small strains, and the shear band orientations are determined by the macroscopic stress state.

Acknowledgements

References

[1] Jang JSC, Koch CC. Scripta Metall Mater 1990;24:1599.
[2] Nieman GW, Weertman JR, Siegel RW. J Mat Res 1991;6:1012.
[3] Siegel RW, Fougere GE. Nanophase materials. Kluwer Academic Publishers, 1993.
[4] He L, Ma E. Nanostruct Mater 1996;7:327.
[5] Carsley JE, Fisher A, Milligan WW, Aifantis EC. Metall Mater Trans A 1998;29A:2261.
[6] Malow TR, Koch CC. Acta Mater 1998;46:6459.
[7] Weertman JR, Farkas D, Hemker KJ, Kung H, Mayo M, Mitra R, Swygenhoven Hv. MRS Bulletin 1999;24:44.
[8] Jia D, Ramesh KT, Ma E. Scripta Mater 2000;42:73.
[9] Legros M, Elliott BR, Rittner MN, Weertman JR, Hemker KJ. Phil Mag A 2000;80:1017.
[10] Takaki S, Kawasaki K, Kimura Y. In: Mishra RS, et al., editors. Ultrafine grained materials. 2000, p. 247.
[11] Valiev RZ, Islamgaliev RK, Alexandrov IV. Prog Mater Sci 2000;45:103.
[12] Sanders PG, Youngdah CJ, Weertman JR. Mater Sci Eng A 1997;234-236:77.

[13] Carsley JE, Milligan WW, Hackney SA, Aifantis EC. Metall Mater Trans A 1995;26A:2479.

[14] Carsley JE. Michigan Technological University, Houghton, MI; 1996.

[15] Valiev RZ, Kozlov EV, Ivanov YF, Lian J, Nazarov AA, Baudelet B. Acta Metall Mater 1994;42:2475.

[16] Suryanarayanan IR, Frey CA, Sastry SML, Waller BE, Buhro WE. Mater Sci Eng A 1999;A264:210.

[17] Jain M, Christman T. Acta Metall Mater 1994;42:1901.

[18] Gray GT, Lowe TC, Cady CM, Valiev RZ, Aleksandrov IV. Nanostructured Materials 1997;9:477.

[19] Malow TR, Koch CC, Miraglia PQ, Murty KL. Mater Sci Eng A 1998;A252:36.

[20] Vinogradov A, Hashimoto S. Mater Trans JIM 2001;42:74.

[21] Dalla Torre F, Swygenhoven HV, Victoria M. Acta Mater 2002;50:3957.

[22] Malow TR, Koch CC. Metall Mater Trans A 1998;29:2285.

[23] He L, Ma E. J Mater Res 1996;11:72.

[24] Jia D. Ph.D. dissertation. Johns Hopkins University, Baltimore, MD; 2001.

[25] Jia D, Ramesh KT. 2002, (submitted).

[26] da Silva MG, Ramesh KT. Int J of Plasticity 1997;13:587.

[27] Zerilli FJ, Armstrong RW. J Appl Phys 1987;61:1816.

[28] Duesbery MS, Vitek V. Acta Mater 1998;46:1481.

[29] Ngan AHW, Wen M. Comput Mater Sci 2002;23:139.

[30] Seeger A, Schiller P. Acta Metall 1962;10:348.

[31] Ono K. J Appl Phys 1968;39:1803.

[32] Kocks UF, Argon AS, Ashby MF. Prog Mater Sci 1975;19:1.

[33] Lennon AM, Ramesh KT. Int J Plast 1998;14:1279.

[34] Tang M, Kubin LP, Canova GR. Acta Mater 1998;46:3221.

[35] Valiev RZ, Aleksandrov IV, Zhu YT, Lowe TC. J Mat Res 2002;17:5.

[36] Wei Q, Jia D, Ramesh KT, Ma E. Appl Phys Lett 2002;81:1240.

[37] Khan AS, Huang S. Int J Plasticity 1992;8:397.

[38] Jia D, Wang Y, Ramesh KT, Ma E, Zhu Y, Valiev R. Appl Phys Lett 2001;79:611.

[39] Koch CC, Morris DG, Lu K, Inoue A. MRS Bulletin 1999;24:54.

[40] Muhlhaus HB, Vardoulakis I. Geotechnique 1987;37:271.

[41] Oda M, Iwashita K. Int J Eng Sci 2000;38:1713.

[42] Milligan WW, Hackney SA, Ke M, Aifantis EC. Nanostruct Mater 1993;2:267.

[43] Schiotz J, Tolla FDD, Jacobsen KW. Nature 1998;391:561.

[44] Fan C, Inoue A. Mater Trans JIM 2000;:1467.

[45] Donovan PE, Stovvs WM. Acta Metall 1981;29:1419.